J Mater Sci (2014) 49:2213–2224
DOI 10.1007/s10853-013-7915-3

Orientation, stress, and strain in an (001) barium titanate single crystal with 90° lamellar domains determined using electron backscatter diffraction

Jane A. Howell · Mark D. Vaudin · Robert F. Cook

Received: 24 September 2013 / Accepted: 24 November 2013 / Published online: 10 December 2013

Abstract The orientation, stress, and strain in a single crystal of barium titanate ($BaTiO_3$), containing relatively large (0.5–14.5 μm), parallel, lamellar domains, have been determined and mapped using electron backscatter diffraction (EBSD). The strain distribution in the single crystal was determined using cross-correlation analysis of the EBSD patterns. Strain in the (001) single crystal was dominated by strain in the minority a-domain bands with peak values of −0.006 determined in the surface plane, perpendicular to the intersection of the domain walls with the crystal surface, compared to +0.002 in the same direction for the majority c-domains. The out-of-plane strains were negatively correlated with the in-plane strains and were about a factor of two smaller. The experimentally determined strains peak at domain boundaries and suggest a contraction of the *c*-axis and an expansion of one of the *a*-axes as the domain wall is approached. The ratios of the in-plane and out-of-plane strains were consistent with the bulk elastic constants of $BaTiO_3$. Stress values determined from the strains and the elastic constants peaked at 400 MPa.

Introduction

The most frequently used passive component in electronic devices is the ceramic capacitor, of which the most common is the multilayer ceramic capacitor (MLCC) [1]. More than 1.5 trillion MLCCs were manufactured in 2009, representing a value of approximately 7 billion US dollars [2]. Given the pervasiveness of MLCC technology, ensuring MLCC reliability is critical for the operation of a multitude of devices. Hence, identifying the failure mechanisms responsible for truncating MLCC reliability is of great importance for optimizing MLCC designs and manufacturing processes and for defining allowed MLCC operating environments. MLCC failure [3–5] can be caused by electrical breakdown of the ceramic dielectric, mechanical failure of the dielectric, or failure of the interface between the dielectric and metallic electrode. In the first two failure cases, microstructural features in the dielectric lead to concentrations of electric field or stress, causing electrical or mechanical failure, respectively. This paper focuses on the second of these, mechanical failure, by identifying microstructural features in the dielectric that lead to stress concentrations. The material investigated is barium titanate ($BaTiO_3$) the most common dielectric material in MLCCs [1, 6]. Results are presented of stress and strain analyses using electron backscatter diffraction (EBSD) for the simplified case of a single crystal of $BaTiO_3$ with large lamellar domains; a domain being a region of invariant direction of electrical polarization. The results provide a basis for interpretation of stress concentration measurements in single crystals with smaller domains, coarse- and fine-grained polycrystalline materials, and MLCCs, as well as a comparison of results obtained from EBSD and confocal Raman microscopy measurements [7, 8].

To date, very few studies have been published regarding EBSD of $BaTiO_3$, and all of the published results have concerned polycrystalline samples [9–14], which focused on domain orientation [9, 10, 12, 14] and texture and grain boundary character [11, 13]. EBSD has also been used to

J. A. Howell · M. D. Vaudin · R. F. Cook (✉)
Materials Measurement Science Division, National Institute of Standards and Technology, Gaithersburg, MD 20899, USA
e-mail: robert.cook@nist.gov

J. A. Howell
e-mail: jane.howell@nist.gov

M. D. Vaudin
e-mail: mark.vaudin@nist.gov

successfully map the orientation of single crystalline samples of $BiFeO_3$–$PbTiO_3$ [15] and $Pb(Mg_{1/3}Nb_{2/3})O_3$-35 mol% $PbTiO_3$ [16]. Similarly, very few studies have been published in which stress or strain has been measured in $BaTiO_3$ samples [17–19], but several studies have been published concerning other ferroelectric materials such as $LiTaO_3$ [20, 21], $LiNbO_3$ [20, 22], $BiFeO_3$ [23], $PbTiO_3$ [24], $Pb[Zr_xTi_{(1-x)}]O_3$ (PZT) [15, 25], and $BiFeO_3$–$PbTiO_3$ [15]. These studies used synchrotron diffraction imaging [20], near-field scanning optical microscopy [21], X-ray topography [22], X-ray microdiffraction [23], EBSD [15], and transmission electron microscopy (TEM) [25] to measure strain. Large values of tensile stress have been inferred at a four domain junction in a herringbone structure in polycrystalline PZT (0.56 GPa using EBSD [15], approaching 1 GPa using TEM [25]) and single crystalline $BiFeO_3$–$PbTiO_3$ (1.4 GPa using EBSD [15]).

At room temperature, the unit cell of $BaTiO_3$ is tetragonal, with the *c*-axis of the unit cell approximately 1.1 % longer than the *a*-axes in an unstrained lattice [25]. As a consequence of this tetragonal distortion, mismatches in lattice parameter occur in the material where unit cell orientation changes, particularly at 90° domain boundaries at which the mismatch is a maximum. As a consequence, to maintain compatibility, strains, and accordingly stresses, develop to accommodate the change in unit cell length across boundaries. Regions of high strain near domain boundaries have been suggested from studies conducted on single crystalline and polycrystalline $BaTiO_3$ using TEM, reflection electron microscopy, atomic force microscopy (AFM), and synchrotron white-beam X-ray topography [27–32]. Strained regions surrounding domain boundaries are also suggested from models [24, 33] and considerations [30, 32] of the crystallographic structure of domains at domain boundaries, which include rotations and distortions of the lattice that increase as the domain wall is approached. Taken together, the studies suggest that 90° domain boundaries in $BaTiO_3$ are a few unit cells in width, approximately one nanometer, with peak strains in the boundary about half the tetragonal distortion. However, the extent of the strain field in the adjacent domains is less clear, with estimates ranging from a few nanometers [24, 33] to a few micrometers [30, 32].

The focus of this paper is the direct, quantitative determination of the variation in strain across a series of parallel c- and a-domains and their boundaries in $BaTiO_3$. EBSD is used in two ways to accomplish this determination: (i) EBSD patterns are indexed to obtain domain orientation; (ii) EBSD patterns are cross-correlated to determine the components of the strain tensor. The following section describes the sample used for the measurements and the measurement methods, including the determination of stress from strain. This is followed by presentation of strain and stress linescans and consideration of the variation of strain with domain size. Finally, a discussion considers the relationships between the crystal structure and the strains within domains and at domain boundaries, a comparison of measured strain component ratios with those predicted from elastic constants, a method to determine orientation from cross-correlation strain measurements for instances where pattern indexing is unclear, and estimation of the flaw sizes required to cause material failure.

Materials and methods

Material

The sample used for all of the experiments was a single crystal of $BaTiO_3$ grown by the Czochralski method. The crystal was in the form of a plate, approximately 4 × 3 mm and 1 mm thick, the bulk of which was oriented with the *c*-axis perpendicular to the surface of the large (*c*-domain) face. Regions near both ends of the sample contained multiple 90° domain boundaries, where the *c*-axis rotated from perpendicular to the surface (*Z*-direction) to parallel to the plane of the surface (*X*-direction). Figure 1 shows two light microscope images of the sample as well as a schematic diagram of the domain region showing the orientation of the *c*-axis as well as the *XYZ* co-ordinate system used throughout the paper. Prior to EBSD analysis, the sample was manually polished with a chemical mechanical polishing solution composed of 2.6 g alumina powder with a diameter of 0.3 μm, 1.6 g NaCl, 5.4 g 30 % hydrogen peroxide, and 30.2 g deionized water. The sample surface was not coated before being loaded into a field emission scanning electron microscope (SEM) (Hitachi S4700 FESEM,[1] Hitachi High-Tech, Tokyo, Japan) for EBSD analysis.

Orientation analysis

The orientation of the single crystal as shown in Fig. 1 was determined from EBSD patterns of the surface. EBSD does not distinguish between 180° rotations of ±c, but for simplicity patterns indexed with the c-axis along the *Z*-direction (c-domain) are shown with the polarization along the positive *Z*-axis, and patterns indexed with the *c*-axis parallel to the *X*-direction (a-domain) are shown with the polarization along the positive *X*-axis. In this scheme,

[1] Certain commercial equipment, instruments, and software are identified in this paper in order to specify the experimental procedure adequately. Such identification is neither intended to imply recommendation or endorsement by the National Institute of Standards and Technology, nor is it intended to imply that the equipment or software identified are necessarily the best available for the purpose.

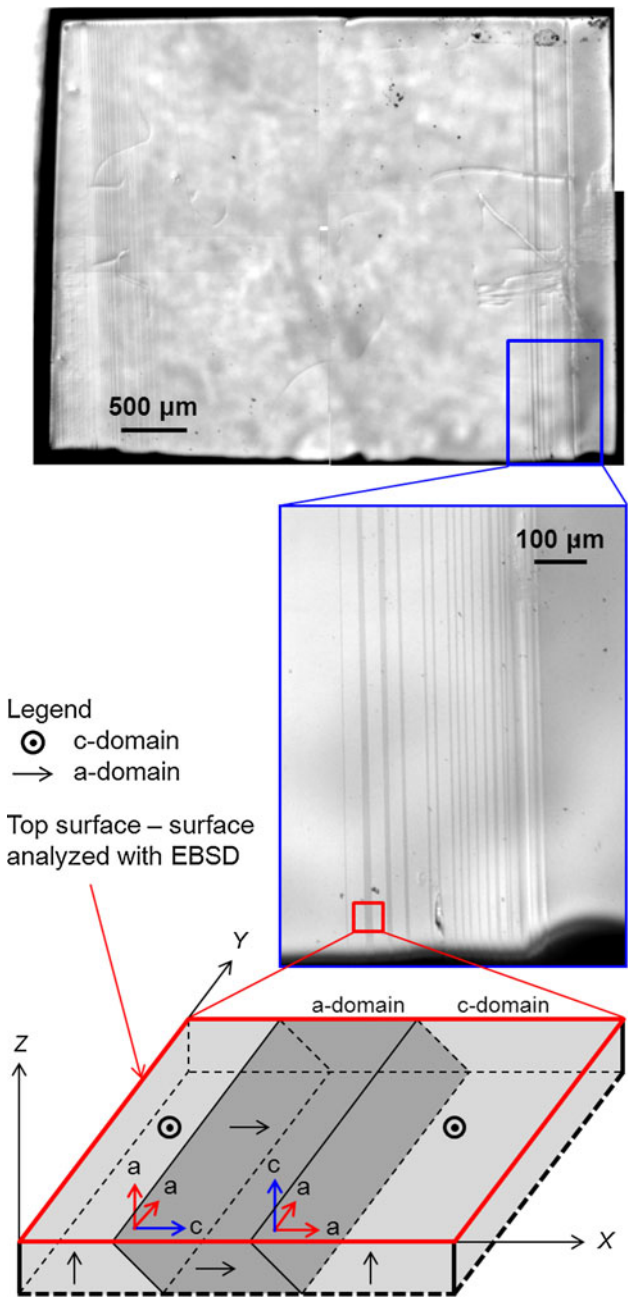

Fig. 1 Light microscope images of the $BaTiO_3$ single crystal (*top*, *middle*) and a schematic diagram of the banded region observed at both ends of the sample (*bottom*). The center region of the crystal was oriented with the *c*-axis perpendicular to the surface (*Z*), while both ends have alternating bands with the *c*-axis perpendicular or parallel to the surface (*X*) (indicated by the black arrows on the *Y* face)

a- and c-domains have their [100] and [001] axes, respectively, parallel to *Z*, and the a-c domain boundaries are (101) planes (relative to c-domain axes) inclined at approximately 45° to *Z*.

EBSD diffraction patterns were recorded with the sample tilted at 70° to the incident electron beam at an accelerating voltage of 20 kV and a beam current of ≈2 nA. An upper bound for the escape depth of the electrons producing the EBSD patterns is 10–40 nm, with experimental values obtained that are as small as 2–6 nm [34, 35]. Lateral resolution is estimated as 50 nm in the *X* direction and 150 nm in the *Y* direction. No binning (image size: 1344 × 1024 pixels) was applied to the EBSD patterns, which were recorded with automatic background subtraction. Typical scans of the $BaTiO_3$ crystal were composed of at least three lines of 200 EBSD patterns; each pattern was recorded in approximately 1 s. The distance between patterns in the *X*-direction was 0.5 μm, with a distance of 5 μm between adjacent lines in the *Y*-direction. Each EBSD pattern was indexed with Oxford HKL Flamenco software (version 5.0.9.1, Oxford Instruments, Abingdon, United Kingdom). Kikuchi band detection was determined with a resolution of the Hough space of 125, using the band edges from a circular region centered on the middle of the pattern with a radius of 511 pixels. Indexing was determined from the automatic detection of five to six bands.

Strain analysis

Entire datasets (typically 600 patterns giving 600 data points) were analyzed for strain using the method of cross-correlation (CrossCourt 3.0, BLG Productions, Bristol, United Kingdom) [36]. Two reference patterns were used in each dataset; one in the center of a c-domain and the second centered in an a-domain. All c-domains were analyzed with the c-domain reference, and all a-domains were analyzed with the a-domain reference. Reference points were chosen from large domains near the center of scans. By definition the reference points are assigned values of zero strain, and thus all values of strain are actually the difference in strain between the reference location and the measurement location. The domain center was chosen as the reference location as the literature results have suggested strain concentrations near domain boundaries [28, 29, 37] and X-ray microdiffraction measurements [18] showed a minimum in strain at the domain center. The tensor strain data (ε_{xx}, ε_{yy}, ε_{zz}, ε_{xy}, ε_{yz}, ε_{xz}) were obtained from analyzing 20 regions of interest [36] (256 × 256 pixels) from each EBSD pattern, and are reported as both interpolated maps of the entire three-line dataset and linescans extracted from the middle row of data. The normal stress, σ_{zz}, was taken as zero as the measurement was regarded as surface-localized (and in fact, this is a condition used in the determination of the strain tensor from the EBSD measurements [36]).

Stress calculations

The strain data were converted to stress (σ) using the appropriate elastic constants for $BaTiO_3$, using (in Voigt

notation) $\sigma_i = C_{ij}\varepsilon_j$. Several different sets of elastic constants are available in the literature [38–41], but the ones of Berlincourt and Jaffe [38], which are those quoted in the CRC Handbook of Chemistry and Physics [42], are used in this study and are given in the C_{ij} stiffness matrix below.

$$C_{ij}(\text{GPa}) = \begin{bmatrix} 275 & 179 & 152 & 0 & 0 & 0 \\ 179 & 275 & 152 & 0 & 0 & 0 \\ 152 & 152 & 165 & 0 & 0 & 0 \\ 0 & 0 & 0 & 54.4 & 0 & 0 \\ 0 & 0 & 0 & 0 & 54.4 & 0 \\ 0 & 0 & 0 & 0 & 0 & 113 \end{bmatrix}$$

The relative uncertainty in a given C_{ij} value is less than 2 % [38], and hence converting strain to stress adds an additional relative uncertainty of 2–3.4 %. As there was a slight misorientation (2°–3°) between the crystallographic axes and the sample axes, the stiffness matrix was rotated by CrossCourt in order to obtain the correct values of stress.

Results

The majority of the data presented in the following sections detail the results from a single scan on the $BaTiO_3$ single crystal containing three lines of 200 data points. Several other scans were obtained from different locations on the same sample, and all gave similar results.

Sample orientation

With a freshly polished surface it is possible with EBSD to clearly distinguish between regions of the single crystal that are oriented with the *c*-axis perpendicular to the surface (c-domains) or parallel to the surface (a-domains). Examples of EBSD patterns with and without the simulated pattern overlay and indexing are shown in Fig. 2 for points in the bands observed on the surface under light microscopy as light and dark regions as seen in Fig. 1. These were identified (computationally) as c-domains (lighter gray) and a-domains (darker gray); the small tetragonal distortion leads to EBSD patterns from the two domain orientations that are extremely difficult to distinguish by eye, as is apparent in Fig. 2. (Although the insets in Fig. 2 indicate axes labeled a, b, and c, EBSD cannot distinguish between a and b as they are equivalent.)

The orientation results from an entire scan bisecting 15 domains are shown in Fig. 3; the carbonaceous deposits left by the three scan lines are apparent. The pattern indexing shown toward the bottom of the SEM image reproduces the banding seen in the SEM image very well, with the darker gray bands having the *c*-axis in the *X*-direction and the lighter gray bands having the *c*-axis in the *Z*-direction, or perpendicular to the surface. There were a few mis-indexed points, which primarily occurred in the domain to the far right where there was increased surface roughness. Excluding the data from this last domain,

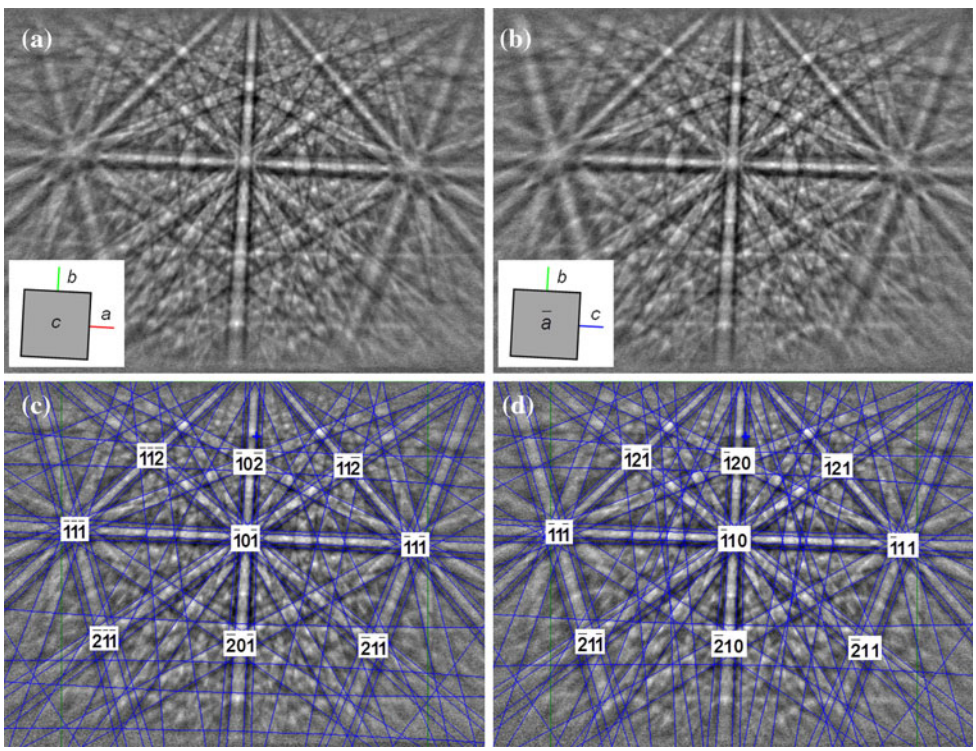

Fig. 2 **a**, **b** EBSD patterns obtained from the $BaTiO_3$ single crystal and **c**, **d** the indexed EBSD patterns in (**a**, **b**). **a** and **c** correspond to a point in a c-domain and **b** and **d** to a point in an a-domain. The insets in **a**, **b** show the different crystallographic orientations

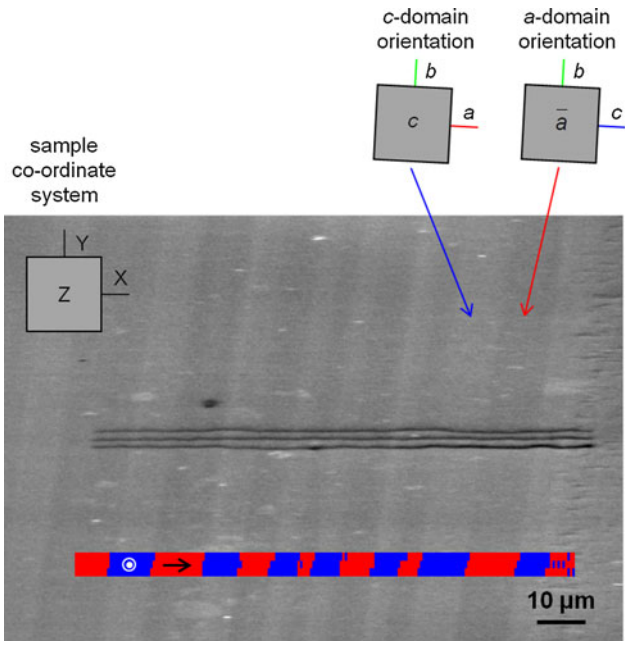

Fig. 3 SEM image of the $BaTiO_3$ single crystal showing the location of an EBSD scan in the center of the image. At the top right of the image is the crystallographic orientation of the sample according to EBSD pattern indexing. Beneath the scan the complete orientation map is shown, with *red* indicating an a-domain and *blue* a c-domain

≈96 % of the data points were indexed correctly. Points were considered to be mis-indexed if an isolated data point had a different direction of the *c*-axis from the surrounding data points. Mis-indexed points could also easily be observed as large abrupt changes in apparent strain with values approaching 1 % (the tetragonal distortion of $BaTiO_3$). A procedure has been developed to confirm the automated indexing, and is presented in the "Discussion". The color scheme shown in the orientation map is used throughout the paper to indicate the different domain orientations (red = a-domain, blue = c-domain).

Also evident in Fig. 3 is a small misorientation between the sample axes (*X*, *Y*, *Z*) and the crystallographic axes of the sample (a, b, c): the light and dark banding of the domains follows crystallographic axes. From an analysis of the Euler angles of the scan it was determined that the crystallographic axes in the plane of the mounted sample were rotated ≈2°–3° clockwise from the *XY*-axes. The misorientation between the *Z*-axis and the out-of-plane crystallographic axis was less than 0.5°.

Strain analysis

The results from the strain analysis of the scan shown in Fig. 3 are shown in Fig. 4 for the normal strain components. The locations of the reference points are indicated by the stars located in the eighth and ninth domains of the top orientation map. The composite strain maps were derived from interpolations of strain component measurements between the three line scans; the colors indicate different levels of strain from compression (dark) to tension (light). The banding in strain closely follows the orientation map, indicating strain consistency between the three scans. The results from the normal strains show considerably more strain in the *X*- and *Z*-directions than in the *Y*-direction and the strain in the *X*- and *Z*-directions mirror one another, *i.e.*, when one is positive the other is negative. The results from the shear strains showed no clear trends across the multiple domain scan. A second scan (not shown) performed just above the data shown in Fig. 4, but with a smaller step size (0.2 μm compared to 0.5 μm) indicated small fluctuations in ε_{yz} and ε_{xz}, although both shear strain components were approximately an order of magnitude less than ε_{xx} and ε_{zz}.

The data from the first half of the middle scan in Fig. 4 are shown in the linescans of Fig. 5a and b; note the change of scale between the normal and shear strains. For the c-domains, the normal strains are near zero across the majority of the domain, becoming positive in the *X*-direction near the domain boundaries, slightly negative in the *Y*-direction near the boundaries, and negative in the *Z*-direction near the boundaries. For the a-domains, the exact

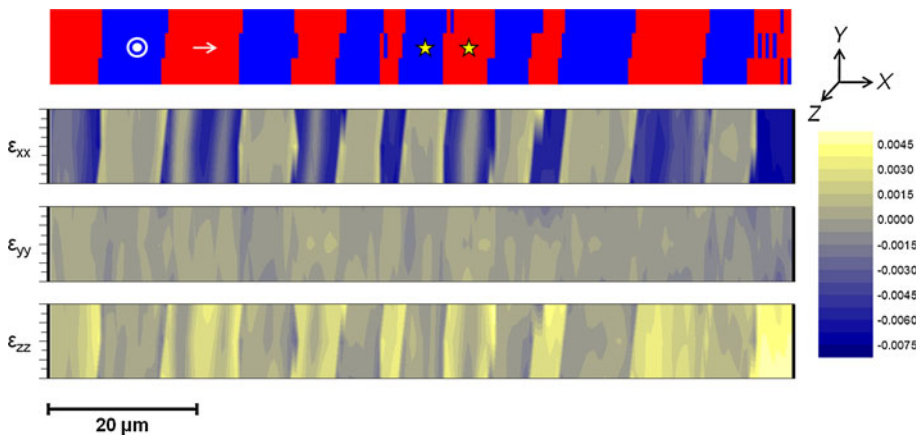

Fig. 4 Normal strains in the *X*-, *Y*-, and *Z*-directions obtained using the cross-correlation method for the scan location shown in Fig. 3. The top image shows the sample orientation, with the arrow and bulls-eye indicating the direction of the *c*-axis and the stars indicating the EBSD reference locations. The maps of strain were generated from interpolation of all three lines of data; the tic marks to the left indicate separations of approximately 2 μm

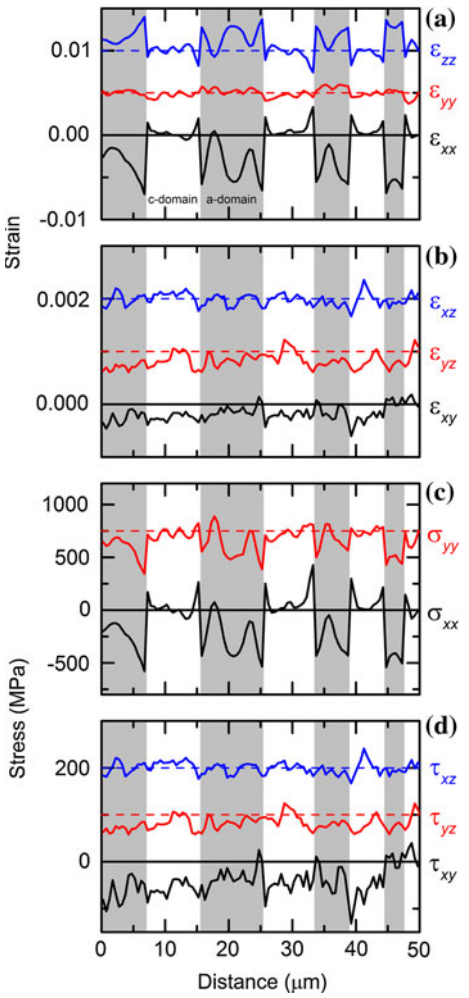

Fig. 5 Line profiles of the **a** normal strains, **b** shear strains, **c** normal stresses, and **d** shear stresses for the first half of the scans shown in Fig. 4 from the middle row of data. For clarity the ε_{yy}, ε_{zz}, ε_{yz}, ε_{xz}, σ_{yy}, τ_{yz}, and τ_{xz} data are offset from zero; the location of zero in these cases is indicated by a dashed line

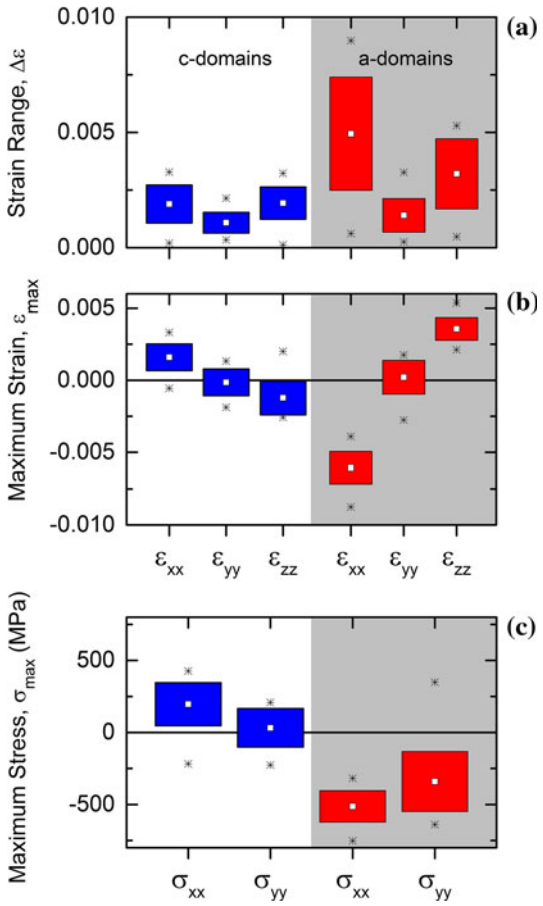

Fig. 6 Normal **a** strain ranges, **b** maximum strains, and **c** maximum stresses measured for domains from scans of three different regions of the $BaTiO_3$ single crystal

opposite trends occur at the boundaries, but with greater values of strain. A slightly different strain profile was noted in one of the a-domains (first full a-domain), which shows peak strains at the domain boundaries as well as at the domain center. This is likely due to a small un-indexed c-domain, or a subsurface c-domain. It is also noted that the strain is not always zero at the domain center in the a-domains, in contrast to the c-domains. For both domain orientations, the peak value of strain is fairly constant across the entire scan.

A summary of the data from three different scan regions of the single crystal, encompassing about 40 domains, is presented in Fig. 6 for the strain range, $\Delta\varepsilon$ (the magnitude of the difference between the maximum and minimum strains in a particular domain), Fig. 6a, and the maximum strain, ε_{max} (the largest numerical value of strain in a particular domain, independent of sign), Fig. 6b, as a function of domain orientation. In the figures, the open square represents the mean value, the filled box shows standard deviations about the mean, and the asterisks indicate maximum and minimum observed quantities. The data clearly show that the a-domains have a greater magnitude of strain than the c-domains, and the sign of strain is opposite for the two domain types. The strain in the *Y*-direction is the smallest of the three strains, and in most cases has the same sign as the strain in the *Z*-direction, which is opposite to the strain in the *X*-direction. The strain and strain range in the *X*-direction are slightly greater than the strain and strain range in the *Z*-direction. As with the maximum strain, the a-domains have a larger strain range than the c-domains, and the largest range values are observed in the *X*- and *Z*-directions.

There is a lot of scatter in the data for the strain range and this is due to the different domain widths observed in the scan area. The strain range data from Fig. 6 are re-plotted in Fig. 7 as a function of the width of the domains. A clear correlation is observed between the strain range and the domain size: as the domain size increases, so does the strain range in the domain. This is more evident in the

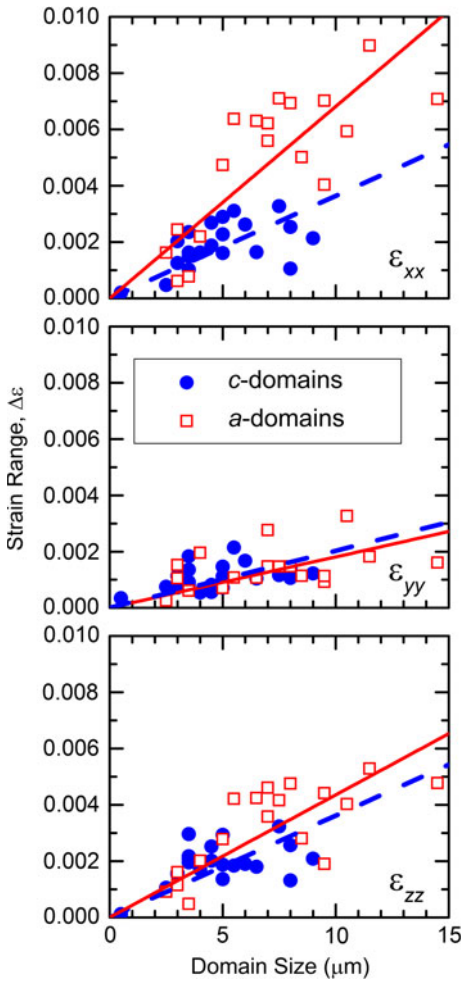

Fig. 7 Normal strain ranges as a function of domain size for the $BaTiO_3$ single crystal using data from the same three scans as in Fig. 6. The *straight lines* are linear fits to the data with enforced zero origin

X- and *Z*-directions and in the a-domains. No observable trend was detected for the maximum strain as a function of domain size.

Stress calculations

The strain data presented in the previous section were converted to stress using the stiffness matrix of $BaTiO_3$. Linescans are shown in Fig. 5c and d for both the normal and shear stresses using the strain data in Fig. 5a and b. The stresses in the $BaTiO_3$ single crystal show trends that are similar to the trends for strain: as was the case for strain, the a-domains have the largest magnitude of stress. The stress is found to be compressive in the *X*- and *Y*-directions in the a-domains and tensile in the *X*- and *Y*-directions in the c-domains. As shown in Fig. 6c, in both domain types the largest stress magnitude is along the *X*-direction, with maximum compressive values of greater than −600 MPa in the a-domains, and +400 MPa tensile values in the c-domains (maximum stress, σ_{max}, is the largest numerical value of stress in a particular domain, independent of sign). Negligible shear stresses were observed in both domain orientations, and in fact τ_{xz} and τ_{yz} should be zero if the assumed conditions of plane stress and surface-localized measurement pertain.

Discussion

Strain within domains

Figures 4 and 5 show that the strain tensor is dominated by strains in the *X* (in plane, parallel to the *c*-axis in a-domains) and *Z* (normal to the plane, parallel to the *c*-axis in c-domains) directions. In the c-domains, strains are tensile in the *X*-direction and compressive in the *Z*-direction, whereas the reverse is true for a-domains. It is also noted that the a-domains have considerably more strain than the c-domains. If we consider the state of strain in an a-domain surrounded by c-domains: As the material transforms from cubic to tetragonal at the Curie temperature, the volume of material in the newly formed a-domain region will attempt to expand along the direction of the *c*-axis (*X*-direction) and contract along the directions of the *a*-axes (*Y*- and *Z*-directions). If there are any constraints in these directions, smaller than equilibrium expansion or contraction will occur and compressive strain in the *X*-direction and tensile strains in the *Y*- and *Z*-directions will result. As there are in fact constraints from the surrounding c-domain material, strains are generated. The opposite strains will occur for a c-domain surrounded by a-domain material. These expected strains are in agreement with the experimental results. As there were no constraints on the contraction in the *Y*-direction, there was very little strain in this direction. The small strain in the c-domains is likely due to the fact that the majority of the crystal is oriented in the c-direction. Previous studies of majority c-domain $BaTiO_3$ crystals [16, 17, 26] also observed considerably more strain and distortion in the minority a-domains, and strains predominantly in the *X*- and *Z*-directions, although in some cases [26] the strain was not quantified. In another case [18], the strain in an isolated a-domain in a c-oriented crystal determined with X-ray microdiffraction was reported as opposite in sign to that here: tensile strain in the *c*-axis direction parallel to the surface and compressive strain in the *a*-axis perpendicular to the surface. The reason for this inconsistency is unclear.

Strain and misorientation at domain boundaries

Although there is variation of strain within domains, the magnitude of the strain rises to a maximum at the domain boundaries, Fig. 5, and is almost invariant with domain size, suggesting that the crystal structure remains the same at each domain boundary regardless of the size of the domain. The consistency of the maximum strain at domain boundaries relative to the strain range within domains is highlighted in Fig. 7. Previous studies, mostly focused on the relative orientation of domains [23–27, 29, 30], have suggested from crystallographic considerations that strain should peak at domain boundaries and that the boundary region should have lattice parameters that approach an average of the a and c unit cell lengths [30] in opposite directions either side of the boundary (assuming no dislocations reduce the lattice coherence). For the boundary between a 90° a–c domain this would result in a contraction of the *c*-axis in the c-domain and an expansion of the *a*-axis in the a-domain, and thus compressive strains would occur in the c-domain along the *c*-axis and tensile strains would be present in the a-domain along the *a*-axis, as observed in Figs. 4, 5, and 6. Figure 5 shows that the strains decrease from the peak values at the domain boundaries as the domain interior is approached. In larger domains, the decrease is almost to zero strain, whereas in smaller domains the decrease is very small; the two right-most a-domains in Fig. 5 are examples of almost full strain decrease and limited strain decrease. As a consequence, the strain range increases with domain size, as shown in Fig. 7. If strain range divided by domain size is taken as an estimate of strain gradient within a domain, the nearly linear variation of strain range with domain size (the fitted lines in Fig. 7) implies that strain gradient is almost invariant with domain size, suggesting that the change in crystal structure as the domain boundaries are approached is also invariant. The relatively rapid reversal of sign of strain gradient at the center of domains suggests that opposing domain boundaries do not sense each other mechanically. For very large domains, the strain and strain gradient should decay to zero as the center of the domain is approached. Inspection of Figs. 5 and 7 suggests that the length scale over which this occurs is about 3–4 μm for the c-domains and about 6–8 μm for the a-domains. Note that the ε_{xx} strain ranges for the larger a-domains in Fig. 7 are of the order of 0.8 %; nearly that of the equilibrium $BaTiO_3$ tetragonal distortion [26], and hence 8 μm could be regarded as an estimate of the length scale over which the strain decreases to zero from the peak strain at a single isolated a-c domain boundary. These length scales are much greater than those observed with TEM [24], but consistent with AFM and X-ray topography observations [30, 32], implying that there may be strain relaxation in unconstrained thin TEM specimens.

Due to the tetragonal distortion, the angle between the c-directions in a- and c-domains deviates slightly from 90°. For an unstrained lattice with lattice parameters of a = 3.992 Å and c = 4.036 Å [26, 41], the deviation from 90° can be determined from geometry to be $\theta = 0.63°$ as given by

$$\theta = 90 - 2\tan^{-1}\frac{a}{c}$$

However, as shown above, the lattice is strained, and deviations from this ideal value could be expected. Several groups have measured this deviation, and those that measure this value close to the boundary typically obtain values less than the expected value of 0.63°. Experimental values have been obtained ranging from 0.35° to 0.60° [30, 43–46]. Preliminary analysis of our data also yields a value less than 0.63°, and a comprehensive analysis of the connection between strain and misorientation at domain boundaries is forthcoming.

Relative magnitudes of strain components

The crystallography discussed in the previous section provides insight into the signs and relations between the strain components, but, apart from an upper bound to the strain (the magnitude of the tetragonal distortion), does not provide quantitative information. Quantitative relations between the strain (and stress) components can be obtained through an analysis of Hooke's law in three dimensions and the elastic constants. For each domain orientation, six equations can be used to describe the relationships between stress and strain (shear terms are ignored as negligible shear was observed in the experiments). In matrix notation these 12 equations can be written as shown below. (The surface is assumed to be under a state of plane stress, and thus σ_{zz} is set to zero, and the small misalignment between the crystallographic and sample axes is not included in this analysis.)

$$\begin{bmatrix}\sigma_{xx}\\ \sigma_{yy}\\ 0\end{bmatrix}_{c-domain} = \begin{bmatrix}C_{11} & C_{12} & C_{13}\\ C_{12} & C_{11} & C_{13}\\ C_{13} & C_{13} & C_{33}\end{bmatrix}\begin{bmatrix}\varepsilon_{xx}\\ \varepsilon_{yy}\\ \varepsilon_{zz}\end{bmatrix}_{c-domain}$$

$$\begin{bmatrix}\varepsilon_{xx}\\ \varepsilon_{yy}\\ \varepsilon_{zz}\end{bmatrix}_{c-domain} = \begin{bmatrix}S_{11} & S_{12} & S_{13}\\ S_{12} & S_{11} & S_{13}\\ S_{13} & S_{13} & S_{33}\end{bmatrix}\begin{bmatrix}\sigma_{xx}\\ \sigma_{yy}\\ 0\end{bmatrix}_{c-domain}$$

$$\begin{bmatrix}\sigma_{xx}\\ \sigma_{yy}\\ 0\end{bmatrix}_{a-domain} = \begin{bmatrix}C_{33} & C_{13} & C_{13}\\ C_{13} & C_{11} & C_{12}\\ C_{13} & C_{13} & C_{11}\end{bmatrix}\begin{bmatrix}\varepsilon_{xx}\\ \varepsilon_{yy}\\ \varepsilon_{zz}\end{bmatrix}_{a-domain}$$

$$\begin{bmatrix}\varepsilon_{xx}\\ \varepsilon_{yy}\\ \varepsilon_{zz}\end{bmatrix}_{a-domain} = \begin{bmatrix}S_{33} & S_{13} & S_{13}\\ S_{13} & S_{11} & S_{12}\\ S_{13} & S_{12} & S_{11}\end{bmatrix}\begin{bmatrix}\sigma_{xx}\\ \sigma_{yy}\\ 0\end{bmatrix}_{a-domain}$$

$\varepsilon_i = S_{ij}\sigma_j$ defines the elastic compliances, S_{ij}. For each domain, the six equations can be combined to provide six ratios of stress and strain, and in particular here, the ratios $\varepsilon_{zz}/\varepsilon_{xx}$ and $\varepsilon_{yy}/\varepsilon_{xx}$ can be predicted and compared with experimental values. For example, using the equation for $\sigma_{zz} = 0$ for the c-domain results in $\varepsilon_{zz}/(\varepsilon_{xx} + \varepsilon_{yy}) = -C_{13}/C_{33}$. Furthermore, if plane strain perpendicular to the Y direction is assumed, as the lamellar domains are very long compared with their lateral dimensions, then $\varepsilon_{yy} \approx 0$ and $\varepsilon_{zz}/\varepsilon_{xx} \approx -C_{13}/C_{33} \approx -0.921$. Using the complete set of equations with no assumptions gives strain ratios of $\varepsilon_{yy}/\varepsilon_{xx}$ (c-domain) $= -0.002$, $\varepsilon_{zz}/\varepsilon_{xx}$ (c-domain) $= -0.920$, $\varepsilon_{yy}/\varepsilon_{xx}$ (a-domain) $= 0.001$, and $\varepsilon_{zz}/\varepsilon_{xx}$ (a-domain) $= -0.553$. A comparison of the expected $\varepsilon_{zz}/\varepsilon_{xx}$ values with the experimental results is shown in Fig. 8, and good agreement between the average experimental and expected ratios is obtained, especially for the a-domains; the larger scatter observed in the c-domains is a consequence of division by small ε_{xx} strain values in these domains. The almost zero $\varepsilon_{yy}/\varepsilon_{xx}$ strain ratios reflect the near plane strain assumption made above and the data of Fig. 5. An assumed double constraint of orthogonal plane stress and plane strain reduces both the shear stress *and* strain components to zero, as was observed here on the long lamellae (Fig. 5) and in measurements on long SiGe mesas [47].

Domain boundary detection using cross-correlation

The automated indexing used to determine the orientation of the $BaTiO_3$ single crystal was able to accurately determine the domain orientation ≈96 % of the time. A method was developed to identify these mis-indexed points, which is especially useful when analyzing samples with smaller domains that may be as small as two to four data points wide. The method used to determine the location of domain boundaries from cross-correlation data is shown in Fig. 9 and relies on treating the tetragonal distortion as an apparent strain.

To determine the location of 90° domain boundaries from EBSD data, the dataset is analyzed using the cross-correlation method as if only a single orientation is present (only one reference point needs to be specified anywhere in the scan region). The resulting strain from this analysis will have bands of small strain, which have the same orientation as the chosen reference point, and bands of much greater strain (approaching 1 % in some instances), which have an orientation 90° from the chosen reference point. The exact cross-over point from one domain type to the next is easily determined by plotting the strain gradient, which shows peaks at the domain boundaries. The domain type (a or c) is determined by the sign of the strain in the high strain bands. If the reference point is chosen such that it is located

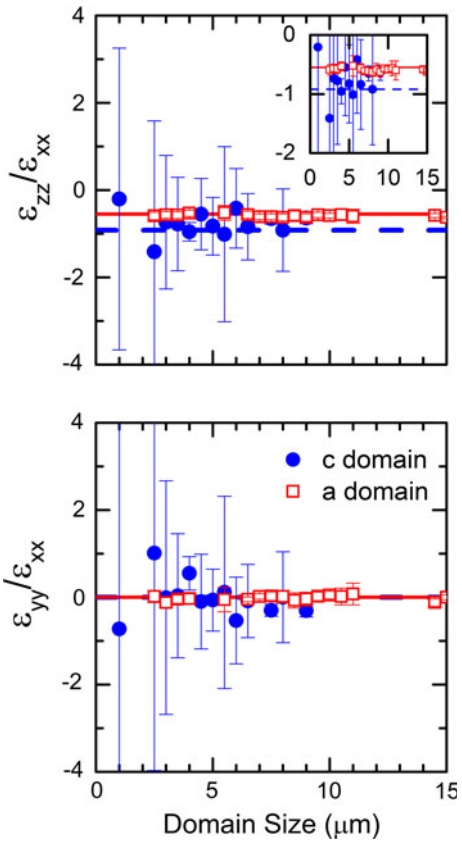

Fig. 8 Strain ratios in the domains as a function of domain size. The ratios were calculated from the values of strain observed at the domain boundaries and were obtained from the same three scans of the $BaTiO_3$ single crystal from Fig. 6. The *horizontal lines* show the strain ratios predicted from bulk $BaTiO_3$ elastic constants

in a c-domain, the strain in the X-direction will be tensile (positive) in the high strain bands (a-domains). This is because in moving from the c-domain to the a-domain, the X-axis is parallel to the short axis of the unit cell, and then parallel to the long axis of the unit cell. When analyzed with a single orientation, this change will be interpreted as a tensile strain. Conversely, if the reference position is located in an a-domain, the high strain bands will be compressive (negative) in the X-direction and this will indicate a transition to c-domains.

Flaw size estimation

Finally, with regard to the overall aim of providing insight into microstructural features that could decrease the mechanical reliability of MLCCs, it is noted that the strains generated at 90° domain boundaries result in considerable stresses, which for the tensile stresses peak at ≈400 MPa in the c-domains. These values are significant, especially considering that the fracture strength, σ_f, of polycrystalline $BaTiO_3$ falls in the range of 90–150 MPa [48, 49]. Using

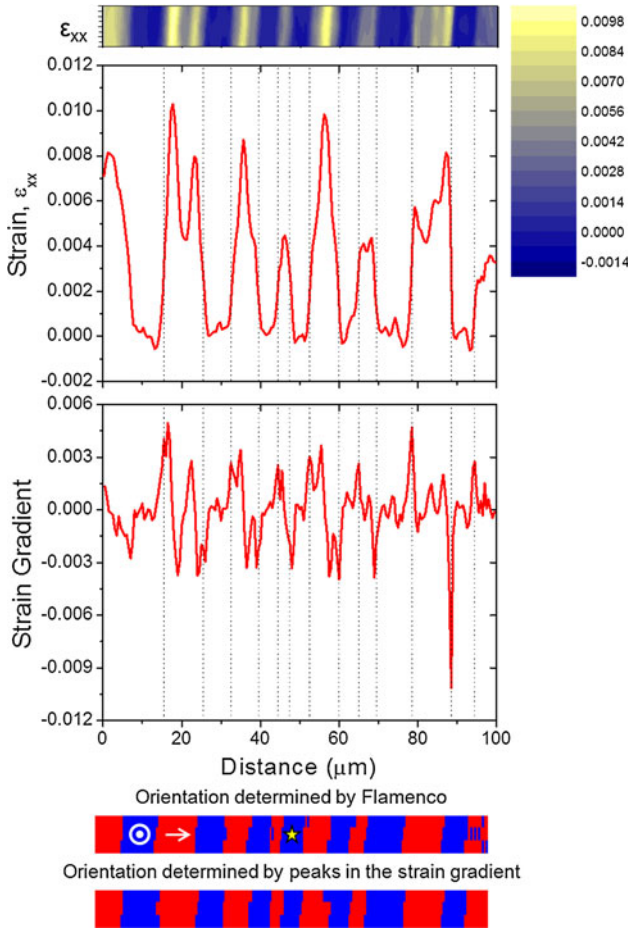

Fig. 9 Illustration of the determination of domain boundary locations from cross-correlation strain data: The apparent strain (*upper*) and strain gradient (*middle*) were obtained using a single reference point shown by the *star* in the orientation map (*lower*). *Dotted lines* show the domain boundaries as determined by pattern indexing. The bottom two images show a comparison of the domain boundaries determined by indexing and by using the peaks in the strain gradient profile

the relation $K_{\mathrm{Ic}} = \sigma_f \sqrt{\pi a}$ and literature values for the fracture toughness of $BaTiO_3$, $K_{\mathrm{Ic}} = (0.7\text{–}1.5)$ MPa $\sqrt{m}$ [49], the flaw sizes required to cause failure in the single crystal examined herein with a peak tensile stress of $\approx$400 MPa can be estimated to be in the range of $a = 1\text{–}5$ μm; no such flaws were observed on the nearly pristine surface. The values of stress and strain in polycrystalline $BaTiO_3$ could be expected to be greater than those observed here, as more complex domain arrangements, such as herringbone and square net patterns [50, 51] are observed, and polycrystalline samples may also have additional strain from the intersection of domains with grain boundaries. However, the insight from the current study is that large stress and strain regions are localized, and hence these regions may well have more influence on crack initiation rather than propagation. However, even small cracks initiated in localized high stress regions, especially adjacent to contacts and interfaces, could lead to MLCC electrical failure. These are topics for future study with EBSD.

Conclusions

The results presented herein demonstrate that high spatial and strain resolution mapping of strain variations in a dielectric, and correlation of those variations with microstructural features, is possible using EBSD cross-correlation techniques. The particular case examined was a ferroelectric $BaTiO_3$ crystal containing parallel, lamellar, alternating a- and c-domains separated by 90° domain boundaries. The strain tensor was dominated by the strain components perpendicular to the crystal surface and perpendicular to the domain boundary intersections with the surface, consistent with the long lamellae being in a state of near plane-strain. The *magnitudes* of the two dominant strain components peaked at the domain boundaries and relaxed toward the domain interiors. The constant values of the maximum strain and relaxation gradient as a function of domain size suggest invariant boundary and near-boundary crystallographic structures. The *signs* of the strain components were consistent with crystallographic considerations of strain compatibility at the domain boundaries, as the $BaTiO_3$ unit cell rotates by 90° and the 1.1 % tetragonal distortion must be accommodated. The state of strain at the domain boundaries is consistent with expansion of the *a*-axis and contraction of the *c*-axis of the unit cell; both deformations were larger in the minority a-domains than in the majority c-domains. The magnitudes of the largest strains observed were approximately 0.8 %, suggesting a spatially distributed domain boundary structure. The *ratios* of the strain components were consistent with bulk elastic constant values. Considerable stresses were associated with the strains, with tensile stresses as great as 400 MPa in some cases. This value is much greater than the typical strengths of polycrystalline $BaTiO_3$ used in MLCCs, suggesting that accommodation of changes in unit cell orientation at domain and grain boundaries in MLCCs could well lead to MLCC failure. The results provide a foundation for extending EBSD mapping of $BaTiO_3$ to smaller and more complicated domain and grain structures and to considerations of domain rotations.

Acknowledgements The authors thank Glen Fox for use of the $BaTiO_3$ single crystal, and Chris Muhlstein for discussions in the early stages of this work.

References

1. Pan MJ, Randall CA (2010) A brief introduction to ceramic capacitors. IEEE Electr Insul Mag 26:44–50
2. Research Summary, In: Capacitor Market 2009, Yano Research Institute Ltd., Tokyo, Japan, 2009, p 4
3. Nomura T (1998) Recent progress of multilayer ceramic capacitors, In: 3rd International Conference on Thin Film Physics and Applications, April 15, 1997, SPIE, Shanghai, China, pp 262–268
4. Rawal BS, Chan NH (2004) Conduction and failure mechanisms in barium titanate based ceramics under highly accelerated conditions. AVX technical information—ceramic capacitors. AVX Corporation, Myrtle Beach, p 7
5. Yang SJ, Kim JW, Ryu DS, Kim MS, Jang JS (2003) Reliability estimation and failure analysis of multilayer ceramic chip capacitors. Int J Mod Phys B 17:1318–1323
6. Reynolds TG III, Buchanan RC (2004) Ceramic capacitor materials. Ceramic materials for electronics. Marcell Dekker, New York, pp 141–206
7. Vaudin MD, Gerbig TB, Stranick SJ, Cook RF (2008) Comparison of nanoscale measurements of strain and stress using electron back scattered diffraction and confocal Raman microscopy. Appl Phys Let 93:193116–1–193116–3
8. Vaudin MD, Stan G, Gerbig YB, Cook RF (2011) High resolution surface morphology measurements using EBSD cross-correlation techniques and AFM. Ultramicroscopy 111:1206–1213
9. Cheng SY, Ho NJ, Lu HY (2006) Crystallographic relationships of the {11–1} growth twins in tetragonal barium titanate determined by electron-backscatter diffraction. J Am Ceram Soc 89:3470–3474
10. Cheng SY, Ho NJ, Lu HY (2008) Polar directions of the 90° and 180° ferroelectric domains in tetragonal barium titanate determined by electron-backscatter diffraction. J Am Ceram Soc 91:1244–1248
11. Ernst F, Mulvihill ML, Kienzle O, Ruhle M (2001) Preferred grain orientation relationships in sintered perovskite ceramics. J Am Ceram Soc 84:1885–1890
12. Koblischka-Veneva A, Mucklich F (2002) Orientation imaging microscopy applied to $BaTiO_3$ Ceramics. Cryst Eng 5:235–242
13. Takahashi H, Numamoto Y, Tani J, Tsurekawa S (2006) Piezoelectric properties of $BaTiO_3$ ceramics with high performance fabricated by microwave sintering. Jpn J Appl Phys Part 1(45):7405–7408
14. Watanabe T, Saito H, Takeda K (2009) Domain observation for BaTiO3 ceramics by a combination of chemical etching and electron backscattered diffraction. Jpn J Appl Phys 48:09KF021–009KF024
15. Farooq MU, Villaurrutia R, MacLaren I, Burnett TL, Comyn TP, Bell AJ, Kungl H, Hoffmann MJ (2008) Electron backscatter diffraction mapping of herringbone domain structures in tetragonal piezoelectrics. J Appl Phys 104:024111–1–024111–8
16. Khan A, Carpenter DT, Scotch AM, Chan HM, Harmer MP (2001) Electron backscatter diffraction analysis of $Pb(Mg_{1/3}Nb_{2/3})O_3$-35 mol% $PbTiO_3$ single crystals grown by seeded polycrystal conversion. J Mater Res 16:694–700
17. Holt M, Hassani K, Sutton M (2005) Microstructure of ferroelectric domains in $BaTiO_3$ observed via X-ray microdiffraction. Phys Rev Lett 95:085504–1–085504–4
18. Rogan RC, Tamura N, Swift GA, Ustundag E (2003) Direct measurement of triaxial strain fields around ferroelectric domains using X-ray microdiffraction. Nat Mater 2:379–381
19. Yamashita Y, Sakakibara S, Yamamoto H, Sakabe Y, Pezzotti G (2005) Micromechanical analysis of fracture and domain switching in barium titanate single crystal using cathodoluminescence piezospectroscopy. J Appl Phys 98:034110–1–034110–12
20. Kim S, Gopalan V, Steiner B (2000) Direct X-ray synchrotron imaging of strains at 180° domain walls in congruent $LiNbO_3$ and $LiTaO_3$ crystals. Appl Phys Lett 77:2051–2053
21. Yang TJ, Mohideen U (1998) Nanoscale measurement of ferroelectric domain wall strain and energy by near-field scanning optical microscopy. Phys Lett A 250:205–210
22. Jach T, Kim S, Gopalan V, Durbin S, Bright D (2004) Long-range strains and the effects of applied field at 180° ferroelectric domain walls in lithium niobate. Phys Rev B 69:064113–1–064113–9
23. Bark CW, Cho KC, Koo YM, Tamura N, Ryu S, Jang HM (2007) Two-dimensional mapping of triaxial strain fields in a multiferroic $BiFeO_3$ thin film using scanning X-ray microdiffraction. Appl Phys Lett 90:102904-1–102904-3
24. Stemmer S, Streiffer SK, Ernst F, Rühle M (1995) Atomistic structure of 90° domain walls in ferroelectric PbTiO3 thin films. Philos Mag A 75:713–724
25. MacLaren I, Schmitt LA, Fuess H, Kungl H, Hoffmann MJ (2005) Experimental measurement of stress at a four-domain junction in lead zirconate titanate. J Appl Phys 97:094102-1–094102-8
26. Kwei GH, Lawson AC, Billinge SJL, Cheong SW (1993) Structures of the ferroelectric phases of barium-titanate. J Phys Chem 97:2368–2377
27. Park BM, Chung SJ, Kim HS, Si WM, Dudley M (1997) Synchrotron white-beam X-ray topography of ferroelectric domains in a $BaTiO_3$ single crystal. Philos Mag A 75:611–620
28. Tsai F, Cowley JM (1992) Observation of ferroelectric domain boundaries in $BaTiO_3$ single crystals by reflection electron microscopy. Ultramicroscopy 45:43–53
29. Tsai F, Khiznichenko V, Cowley JM (1992) High-resolution electron microscopy of 90° ferroelectric domain boundaries in barium titanate ($BaTiO_3$) and lead zirconate titanate ($Pb(Zr_{0.52}Ti_{0.48})O_3$). Ultramicroscopy 45:55–63
30. Takashige M, Hamazaki S, Takahashi Y, Shimizu F, Yamaguchi T (1999) Temperature dependent surface images of $BaTiO_3$ observed by atomic force microscopy. Jpn J Appl Phys Part 1(38):5686–5688
31. Yakunin SI, Shakmano Vv, Spivak GV, Vasileva NV (1972) Microstructure of domains and domain walls in single-crystal films of barium titanate. Sov Phys-Sol State 14:310–313
32. Yoneda Y, Kohmura Y, Suzuki Y, Hamazaki S, Takashige M (2004) X-ray diffraction topography on a $BaTiO_3$ crystal. J Phys Soc Jpn 73:1050–1053
33. Cao WW, Cross LE (1991) Theory of tetragonal twin structures in ferroelectric perovskites with a first-order phase transition. Phys Rev B 44:5–12
34. Dingley D (2004) Progressive steps in the development of electron backscatter diffraction and orientation imaging microscopy. J Microsc 213:214–224
35. Zaefferer S (2007) On the formation mechanisms, spatial resolution and intensity of backscatter Kikuchi patterns. Ultramicroscopy 107:254–266
36. Wilkinson AJ, Meaden G, Dingley DJ (2006) High resolution mapping of strains and rotations using electron backscatter diffraction. Mater Sci Technol 22:1271–1278
37. Yoneda Y, Kohmura Y, Suzuki Y, Morimura R, Kojima A, Mizuki J (2007) Direct observation of non-strain-free style domain in $BaTiO_3$ crystal by synchrotron X-ray topography. Trans Mater Res Soc Jpn 32:31–34
38. Berlincourt D, Jaffe H (1958) Elastic and piezoelectric coefficients of single-crystal barium titanate. Phys Rev 111:143–148
39. Li Z, Grimsditch M, Foster CM, Chan SK (1996) Dielectric and elastic properties of ferroelectric materials at elevated temperature. J Phys Chem Solids 57:1433–1438

40. Schaefer A, Schmitt H, Dorr A (1986) Elastic and piezoelectric coefficients of TSSG barium titanate single crystals. Ferroelectrics 69:253–266
41. Wang JJ, Meng FY, Ma XQ, Xu MX, Chen LQ (2010) Lattice, elastic, polarization, and electrostrictive properties of $BaTiO_3$ from first-principles. J Appl Phys 108:034107–1–034107–6
42. Frederikse HPR (2011) Elastic constants of single crystals. CRC handbook of chemistry and physics: internet version. CRC Press, Cleveland
43. Balakumar S, Xu JB, Ma JX, Ganesamoorthy S, Wilson IH (1997) Surface morphology of ferroelectric domains in $BaTiO_3$ single crystals: an atomic force microscope study. Jpn J Appl Phys, Part 1 36:5566–5569
44. Kalinin SV, Bonnell DA (2000) Effect of phase transition on the surface potential of the $BaTiO_3$ (100) surface by variable temperature scanning surface potential microscopy. J Appl Phys 87:3950–3957
45. Nakahara H, Kaku S, Minakuchi T (2010) Observation of ferroelectric domains having atomically ordered surface in air by atomic force microscopy and piezoresponse force microscopy. Ferroelectrics 401:192–195
46. Tai RZ, Namikawa K, Kishimoto M, Tanaka M, Sukegawa K, Hasegawa N, Kawachi T, Kado M, Lu P, Nagashima K, Daido H, Maruyama H, Sawada A, Ando M, Kato Y (2002) Picosecond snapshot of the speckles from ferroelectric $BaTiO_3$ by means of X-ray lasers. Phys Rev Lett 89:257602-1-4
47. Wilkinson AJ (2006) High resolution measurements of strain and tilt distributions in SiGe mesas using electron backscatter diffraction. Appl Phys Lett 89:241910-1–241910-3
48. Cook RF, Lawn BR, Fairbanks CJ (1985) Microstructure-strength properties in ceramics. I. Effect of crack size on toughness. J Am Ceram Soc 68:604–615
49. de With G (1993) Structural integrity of ceramic multilayer capacitor materials and ceramic multilayer capacitors. J Eur Ceram Soc 12:323–336
50. Arlt G (1990) The influence of microstructure on the properties of ferroelectric ceramics. Ferroelectrics 104:217–227
51. Arlt G, Sasko P (1980) Domain configuration and equilibrium size of domains in $BaTiO_3$ ceramics. J Appl Phys 51:4956–4960